

## Article

# The Cerium/Boron Insertion Impact in Anatase Nano-Structures on the Photo-Electrochemical and Photocatalytic Response

Aurora A. Flores-Caballero <sup>1,2</sup> , Arturo Manzo-Robledo <sup>1</sup> and Nicolas Alonso-Vante <sup>2,\*</sup> 

<sup>1</sup> Instituto Politécnico Nacional, Laboratorio de Electroquímica y Corrosión, Departamento de Ingeniería Química, Escuela Superior de Ingeniería Química e Industrias Extractivas (ESIQIE)-IPN, 07738 Distrito Federal, Mexico; floresca-a@outlook.com (A.A.F.-C.); amanzor@ipn.mx (A.M.-R.)

<sup>2</sup> IC2MP-UMR-CNRS 7285, Department of Chemistry, University of Poitiers, 4 rue Michel Brunet, F-86072 Poitiers CEDEX 9, France

\* Correspondence: nicolas.alonso.vante@univ-poitiers.fr

**Abstract:** Boron- and cerium-doped titania (Anatase) were prepared via sol-gel method. Phase composition and morphology were assessed by X-ray diffraction (XRD), scanning electronic microscopy (SEM), BET, diffuse reflectance spectra (DRS), and XPS. Photo-electrochemistry of these materials, deposited onto fluorine-doped SnO<sub>2</sub> (FTO), was investigated in acid and acid-containing methanol. The boron-doped sample showed the best opto-electronic properties among the investigated samples. On the other hand, the cerium-doped titania samples annihilate to a certain extent the titania surface states, however, photogenerated charge separation was limited, and certainly associated to surface Ce<sup>3+</sup>/Ce<sup>4+</sup> species. The substitutional effect of boron ions for O sites and interstitial sites was confirmed by XRD and XPS analyses.

**Keywords:** doping effect; photo-electrochemistry; photocatalysis; recombination



**Citation:** Flores-Caballero, A.A.; Manzo-Robledo, A.; Alonso-Vante, N. The Cerium/Boron Insertion Impact in Anatase Nano-Structures on the Photo-Electrochemical and Photocatalytic Response. *Surfaces* **2021**, *4*, 54–65. <https://doi.org/10.3390/surfaces4010008>

Academic Editor: Gaetano Granozzi

Received: 23 December 2020

Accepted: 2 February 2021

Published: 15 February 2021

**Publisher's Note:** MDPI stays neutral with regard to jurisdictional claims in published maps and institutional affiliations.



**Copyright:** © 2021 by the authors. Licensee MDPI, Basel, Switzerland. This article is an open access article distributed under the terms and conditions of the Creative Commons Attribution (CC BY) license (<https://creativecommons.org/licenses/by/4.0/>).

## 1. Introduction

New technologies are focused on the study of reactions and fuel generation, where the conversion of solar energy considers fuels such as hydrogen, methanol, methane, and others [1,2]. According to recent reports, hydrogen production is a high-impact process compared to, for example, fossil sources that contribute to the greenhouse effect [3,4]. Semiconductor materials, such as TiO<sub>2</sub>, have been investigated using water photolysis, either photocatalytic or photo-electrocatalytic for the purpose of producing hydrogen [5–7]. Other studies described the TiO<sub>2</sub> as a catalyst with good chemical stability, low cost, and low toxicity [8]. In addition to hydrogen production, TiO<sub>2</sub> is used as a solar protector, advanced devices in optoelectronics, photovoltaic cells, and in the industry, as sensors, pigments, degradation of organic compounds in water effluents [9–12]. The pristine TiO<sub>2</sub> is only active under UV-irradiation, however, several studies were focused on the design of hetero-structures, taking into account the energy band alignment of TiO<sub>2</sub> as a main objective [13,14]. This latter is an important factor that involves optical, physicochemical, and textural properties related to charge carrier separation and charge transfer processes at the semiconductor-electrolyte (SC/El) interface. Another important issue is the positions of the relative energy bands with respect to the energy levels of some selected redox potentials in aqueous electrolyte [12,13,15]. In this context, several preparation techniques such as impregnation, co-precipitation, colloidal, solvothermal, and sol-gel have been employed to synthesize and modify the crystalline properties of TiO<sub>2</sub> through dopants and co-catalysts in order to adapt the electronic states and response in the visible region [16–18]. Some dopant ions and oxides employed, e.g., La<sup>+</sup>, Sm<sup>+</sup>, Ce<sup>+</sup>, In<sup>+</sup>, Eu<sup>+</sup>, Ga<sup>+</sup>, B, N, S, WO<sub>3</sub>, ZnO, could influence the nucleation and growth of TiO<sub>2</sub> crystals improving the photo-electrochemical activity [18,19]. Thus, cerium-based oxides compounds have received a lot of attention because of the redox couple Ce<sup>4+</sup>/Ce<sup>3+</sup> has the ability to exchange, during bias

potential, CeO<sub>2</sub> and Ce<sub>2</sub>O<sub>3</sub> chemical states [20–24]. The easy formation of available oxygen vacancies (OV) in the presence of boron species with a relative high mobility of oxygen species in the bulk has been reported [13,25–29].

The objective of this work was to evaluate the TiO<sub>2</sub> modified by boron and cerium species to reduce recombination rates through doping of TiO<sub>2</sub>. In particular, the results were focused on the charge carrier separation (e<sup>-</sup>/h<sup>+</sup>) in acid conditions and methanol containing acid solution to evaluate the electron accumulation or current enhancing effect and how this phenomenon affects photocatalysis.

## 2. Materials and Methods

### 2.1. Synthesis of Samples

TiO<sub>2</sub> nanoparticles (NPs) and doped-TiO<sub>2</sub> NPs were synthesized by the sol-gel route. The pH was fixed at 3.8. Briefly, titanium butoxide (97% Sigma Aldrich, St. Louis, MO, USA) was added dropwise in ethanol (solution A) under argon atmosphere. Subsequently, a solution B containing 3 mL of CH<sub>3</sub>COOH, 35 mL of ethanol, and 15 mL of H<sub>2</sub>O was prepared and mixed with solution A under stirring conditions for 20 min at room temperature. Then, 2 wt.% of cerium nitrate-hexahydrate (Sigma Aldrich) and 2 wt.% of boric acid H<sub>3</sub>BO<sub>4</sub> (Fluka) were dissolved separately in 10 mL of deionized water, added, and kept under stirring for 24 h at room temperature at a pH = 4.8. The powder was recovered after solvent evaporation at 100 °C and calcined at 400 °C [28]. Samples were labeled: TiO<sub>2</sub>, TiO<sub>2</sub>-B, and TiO<sub>2</sub>-Ce.

### 2.2. Physicochemical Characterization

The morphological and structural properties were characterized using a scanning electron microscopy (JEOL JSM 6701F, JEOL, Peabody, MA, USA) operating at 5.0 kV and a Mini Flex Rigaku X-ray diffractometer model 600 with Cu-K<sub>α</sub> radiation ( $\lambda = 1.54 \text{ \AA}$ ) at 40 kV and 15 mA. The configuration of this equipment was Bragg-Brentano, with a goniometer radius of 15 cm, provided with a Ni filter for K<sub>β</sub> of 0.03 of the radiation from the Cu tube. At the tube exit and before the detector entrance, there are 5° Soller gratings. The slit in the incident optics was 0.625 degrees. In the detector, the slit was 8 degrees because of the ultra-fast detector with that aperture. The Rietveld refinement (RF) calculations were performed by using the COD database 1,010,942 for TiO<sub>2</sub>, Anatase phase [30]. No other phases were detected. Table S1 summarizes the structural properties. The powder-UV spectra were recorded in a Cary 100 Scan UV-Vis Varian apparatus, equipped with an integrating sphere. The surface area was measured with a Quantachrome Autosorb-313 using the Brunauer–Emmett–Teller (BET) method. X-ray photoelectron spectroscopy analysis was carried out using a K<sub>α</sub> Thermo Fischer Scientific spectrometer with a monochromatic Al-k<sub>α</sub> (1486.6 eV) with a resolution of 0.2 eV, vacuum pressure 10<sup>-9</sup> mbar, and analyzed area of 400 μm<sup>-2</sup>. Samples remained at vacuum for more than 10 h in a prechamber directly connected to the equipment and later transferred to the analysis chamber at a base pressure of 1 × 10<sup>-9</sup> Torr. The pass energy for the survey and high-resolution spectra was set to 160 and 45 eV, respectively. The Ti 2p peak at 458.7 eV was used as internal standard to compensate the effects related to charge shift. XPS spectra data were deconvoluted with AVANTAGE V5.97 software from Thermo Fisher Scientific using a Shirley-type background subtraction and a pseudo-Voigt function with Gaussian (70%)-Lorentzian (30%) for each component.

### 2.3. Electrode Preparation

Fluorine-doped tin oxide (FTO) glass (SOLEMS, 70-90 Ohm/sq) was employed as a conductive support with area of ca. 0.9 cm<sup>2</sup>. The FTO plates were cleaned using H<sub>2</sub>O<sub>2</sub>/H<sub>2</sub>SO<sub>4</sub> solution 1/3 (v/v) for 90 min and rinsed for 10 min with ultra-pure water (milliQ). Then, they were dried for 120 min at 90 °C and stocked in a Petri dish. A TiO<sub>2</sub> suspension was prepared with 20 mg of TiO<sub>2</sub> ultrasonically dispersed in 1 mL isopropanol for 20 min at room temperature. An aliquot of 100 μL was drop casted at 5000 rpm. This step was repeated several times and finally TiO<sub>2</sub>/FTO and TiO<sub>2</sub>-B or TiO<sub>2</sub>-Ce/FTO

were heat-treated at 400 °C for 1 h in air atmosphere [31]. The deposited mass was ca. 0.2 mg/cm<sup>2</sup>.

#### 2.4. Electrochemical Measurements

A standard three-electrode electrochemical-cell was employed with the semiconducting materials as working electrodes; RHE and a graphite rod were used as a reference and counter electrode, respectively. The potential was controlled by a BioLogic Bi-Potentiostat and a Princeton Applied Research potentiostat for the photo-electrochemical and electrochemical impedance spectroscopy. The base electrolyte solution was 0.5 M H<sub>2</sub>SO<sub>4</sub> (pH = 0.27). The measurements were carried out in nitrogen-saturated electrolyte containing 0.5 M methanol in a 20 mL cell volume. The potential interval used was from −0.15 to 1.0 V/RHE. Current-potential characteristics were obtained at 1 mV/s. Photocurrent versus time profiles were measured under chopped light with a frequency of 0.1 Hz during 180 s at 0.6 V/RHE. The open circuit potential (OCP) was monitored during 15 min in dark and under illumination conditions. The incident photon to current efficiency (IPCE) was measured in acid media containing 0.5 M methanol, from 300 to 620 nm with 1 nm/s at 0.6 V/RHE during 320 s. The light source (30.8 mW/cm<sup>2</sup>) was provided by an UV-Vis Lamp (Spectral products Model ABB-Xe-175).

#### 2.5. Photocatalysis

Photocatalytic experiments were carried out in a glass cell using, respectively, 20 mg of TiO<sub>2</sub>; TiO<sub>2</sub>-B, and TiO<sub>2</sub>-Ce to evaluate the photooxidation, in presence of oxygen flow, of 40 mg/L Azo dye (Reactive Black 5-RB5), C<sub>26</sub>H<sub>21</sub>N<sub>5</sub>Na<sub>4</sub>O<sub>19</sub>S<sub>6</sub> 2-(4-Aminophenylsulfonyl) ethyl hydrogen sulfate, MW = 991.82 g/mol). The change of the solution absorbance was measured by a UV-Vis Spectrophotometer (Thermo Scientific OMEGA UV/VIS Spectrophotometer). A Xe lamp (300 W) was used as a light UV-Vis source.

### 3. Results and Discussion

#### 3.1. Physical-Chemical Properties

**XRD Analysis**—The powder X-ray diffraction patterns of sol-gel generated samples: TiO<sub>2</sub>, TiO<sub>2</sub>-B, and TiO<sub>2</sub>-Ce are shown in the Supplementary Information (SI), Figure S1. No traces of Rutile phase (JCPDS 0021-1276) or any other species related to cerium or boron oxides were detected by XRD [27,28,32,33]. The absence in the XRD spectra of cerium and or boron species can be due to either an amount below the level of detection of the technique, or to the presence of a highly disordered state of B, Ce species. All diffraction peaks correspond to polycrystalline TiO<sub>2</sub> Anatase phase (JCPDP 001-021-1272).

Rietveld analysis performed on sol-gel generated: TiO<sub>2</sub>, TiO<sub>2</sub>-B, and TiO<sub>2</sub>-Ce, revealed that the doping process of boron and cerium impact the Anatase structure, in three ways, namely, (i) an increase in the size of the crystallite; (ii) an increase in the volume of the unit cell; and (iii) an increase in the microstrain, see fitted structural data in Table S1. These effects are certainly at the origin of the slight positive shift of the Bragg angle observed, as exemplified on the (101) diffraction peak, Figure 1a. This phenomenon can be rationalized via the doping process that might occur by the occupation of octahedral interstitial site or substitutional position of Ti<sup>(IV)</sup> in the anatase lattice. Therefore, with a coordination number of 6, the difference in the ionic radius of B and Ce with respect to Ti<sup>(IV)</sup> ( $r_i = 0.61 \text{ \AA}$ ), in the lattice, is B<sup>(III)</sup> ( $r_i = 0.27$ ) and Ce<sup>(III)</sup>/Ce<sup>(IV)</sup> ( $r_i = 1.01/0.87$ ). The materials perturbation is higher in presence of Ce<sup>(III)</sup>/Ce<sup>(IV)</sup>, since the microstrain in TiO<sub>2</sub>-Ce increased by 17% compared to TiO<sub>2</sub>, see Table S1, on the one hand, and on the other hand, the crystallite size is slightly inhibited, probably due to the crystal growth inhibition and diffusion of Ce-species into the TiO<sub>2</sub> lattice during synthesis [23,33,34], leading to the formation of ceria (Ce<sub>2</sub>O<sub>3</sub>), see XPS section, present in the grain boundaries producing nano-heterojunctions. Therefore, cerium species can be either located in the TiO<sub>2</sub> lattice or at the surface [35]. One further observes that the doping effect by B and Ce is beneficial to enhance the surface area of the samples, see Figure 1b [20,32,36]. All samples present IV and V type isotherms BET

analysis [37–39], corresponding to mesoporous solids under a hysteresis H1-type [40–42]. The diameter of the pores varied from 4 to 6 nm, Figure 1c. The calculated specific surface area determined from the N<sub>2</sub> adsorption-desorption isotherms via BET and pore size are summarized in Table 1.

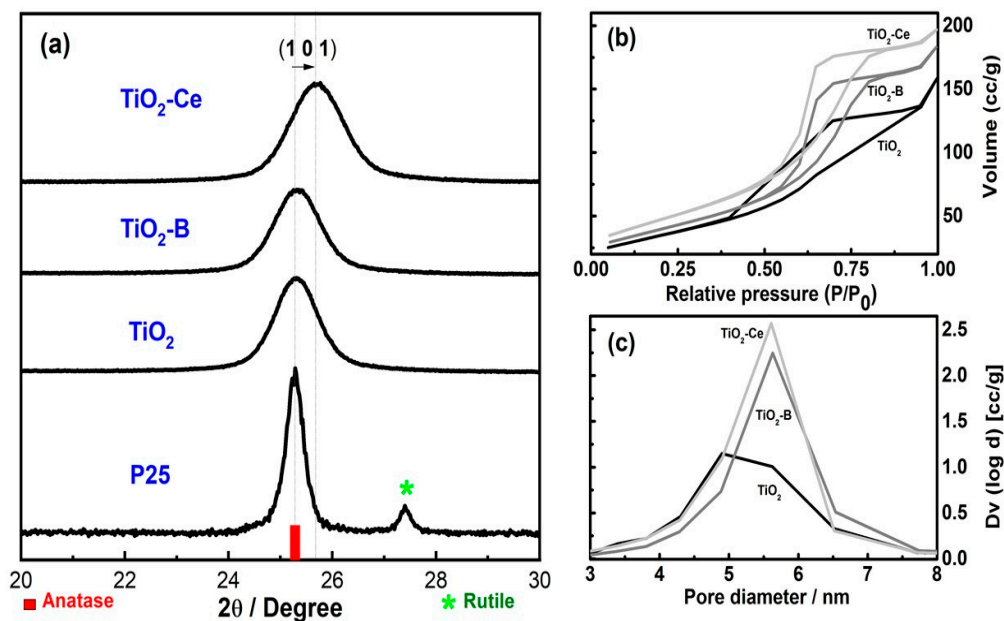


**Figure 1.** (a) The (101) pXRD of sol-gel synthesized samples (TiO<sub>2</sub>, TiO<sub>2</sub>-B, and TiO<sub>2</sub>-Ce). P25 is the reference. (b) BET analysis for nitrogen adsorption-desorption, and (c) pore diameter distribution.

**SEM Analysis**—SEM analyses revealed that the morphology of the samples is that of spheres with rather irregular shapes compared to P25 (from Sigma Aldrich). On the other hand, TiO<sub>2</sub>-B sample shows a rather homogeneous dispersion of the particles compared to TiO<sub>2</sub>-Ce. In fact, the morphology, of the oxide particles, is affected on the surface by the presence of the B and/or Ce species. SEM images of the sol-gel generated samples: TiO<sub>2</sub>, TiO<sub>2</sub>-B, and TiO<sub>2</sub>-Ce are shown in the Supplementary Information (SI), Figure S2.

**Optical Absorption Analysis**—The Kubelka–Munk function deduced from the diffuse reflectance spectroscopy (DRS), is shown in Figure 2a. Tauc’s analysis, Figure 2b, data from Figure 2a, provides the band gap energy,  $E_g$  [43,44]. In agreement with the literature,  $E_g$  (TiO<sub>2</sub> Anatase) was 3.35 eV [36,45]. The TiO<sub>2</sub>-B sample shows a slight absorption in the visible region, whereas the TiO<sub>2</sub>-Ce sample presented an extended threshold in the same region.  $E_g$  for TiO<sub>2</sub>-B and TiO<sub>2</sub>-Ce are 3.30 and 3.2 eV, respectively [46,47]. The absorption threshold in the visible region assesses that boron and cerium species in the titanium dioxide lattice modify the optoelectronic properties of TiO<sub>2</sub>, Table 1.

**XPS Analysis**—The survey XPS spectra (an average of three measurements in different points of each sample) of all oxide samples, Figure S3, and the high-resolution spectra for Ti 2p, and O 1s, C 1s, and Na 1s are shown in Figure 3. The presence of carbon is due the adventitious carbon, whereas Na, and traces of Al<sub>2</sub>O<sub>3</sub>, are due to impurities from the chemical synthesis route. The deconvoluted high resolution spectra for Ti 2p is shown in Figure 3a.

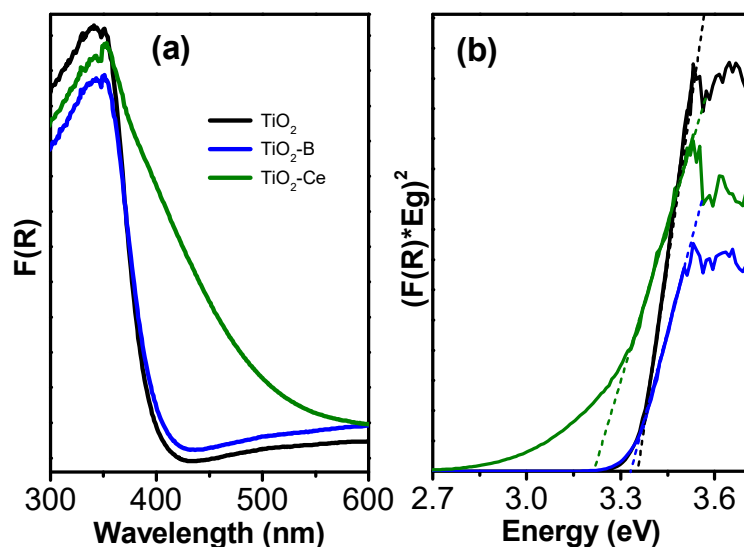


Figure 2. (a) The Kubelka–Munk function ( $F(R)$ ) spectra for B-, Ce-modified  $\text{TiO}_2$  nanoparticles heat-treated at  $400^\circ\text{C}$ . (b) Tauc-plot for an indirect electronic transition of B-, Ce- $\text{TiO}_2$ , and  $\text{TiO}_2$ .

Table 1. Physicochemical and textural properties, and band-gap energy.

Sample	Surface Area BET ( $\text{m}^2\text{g}^{-1}$ )	Pore Size (nm)	Band-Gap (eV)
Degussa P-25	56	1.75 [48]	3.15
$\text{TiO}_2$	128	5	3.35
$\text{TiO}_2\text{-B}$	146	5.63	3.32
$\text{TiO}_2\text{-Ce}$	173	5.59	3.20

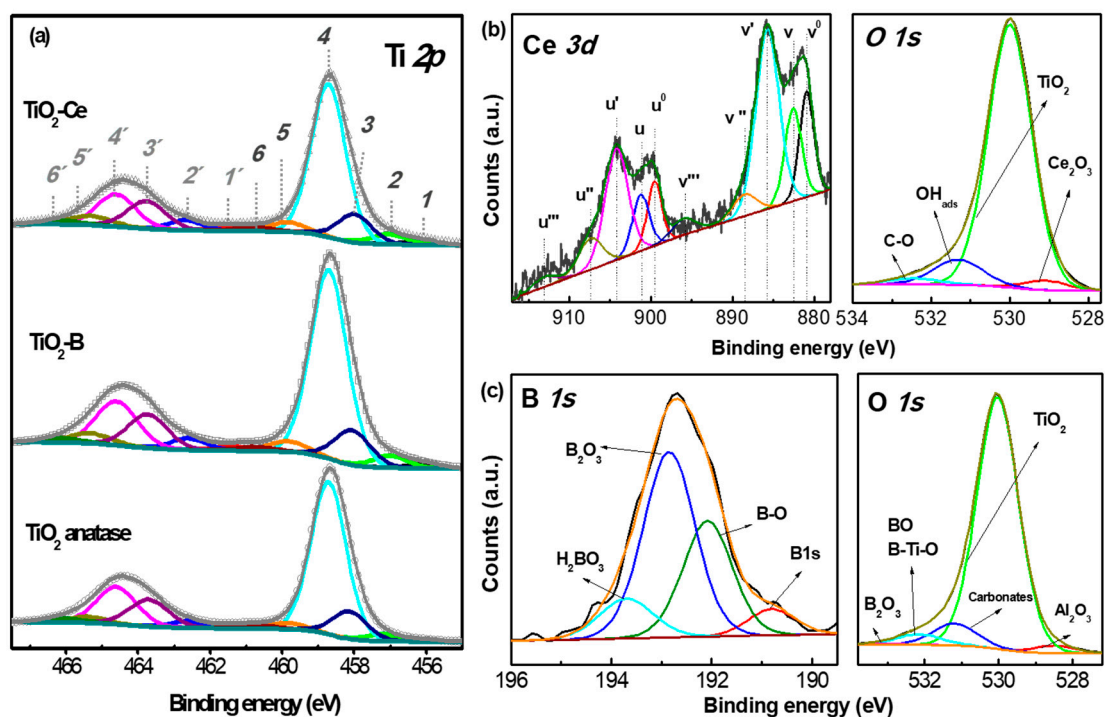


Figure 3. High-resolution XPS spectra (a) Deconvoluted Ti 2p spectra:  $\text{TiO}_2$  anatase,  $\text{TiO}_2\text{-B}$ , and  $\text{TiO}_2\text{-Ce}$  samples. (b) Ce 3d with O 1s, and (c) B 1s regions including the O 1s spectra.

The Ti 2p<sub>3/2</sub> and Ti 2p<sub>1/2</sub> well-resolved peaks with binding energies of 456 and 456.99 ± 0.2 eV assigned to Ti<sup>2+</sup>/Ti<sup>3+</sup> present on the samples. The binding energy centered at 458 ± 0.2 eV can be attributed to boron and cerium interactions within the TiO<sub>2</sub> lattice, as described by Rtimi et al. [49]. Thus, the Van der Waals forces coexist between TiO<sub>2</sub> structure and dopant agents to promote the TiO peak at 458 eV as a result of the dispersion of cerium and boron ions [50,51]. The Ti 2p peak located at 458.71 ± 0.2 eV is attributed to Ti–O bonds in Ti<sup>4+</sup> oxidation state [52,53]. Other contributions of TiO(OH)<sub>2</sub> species at 459.85 ± 0.2 eV, related to the alkoxide conversion to the “sol” and other OH species adsorbed during synthesis, were also detected, which increased with cerium dopant due to the ion interaction with TiO<sub>2</sub> lattice [54].

In addition, a small contribution of Ti–C was also found at 460.75 ± 0.2 eV. Besides, the “shake down” states of peaks, labeled 1' to 6', are the result of energy gain processes and photoelectron emission. In this way, Figure 3b,c shows the Ce 3d, B 1s, and O 1s spectra deconvolution. In the Ce 3d spectra, Ce<sup>3+</sup> was detected at 885.7 ± 0.2 eV as a result of Ce<sub>2</sub>O<sub>3</sub> formed at the TiO<sub>2</sub>-surface with respect to Ce<sup>4+</sup> at 882.55 ± 0.2 eV [47]. The binding energies of compounds at v<sup>0</sup>, v', u<sup>0</sup>, and u' are related to Ce<sup>3+</sup> species. Herein, u' and v' peaks represent Ce 3d<sup>9</sup> 4f<sup>1</sup> O 2p<sup>6</sup> as final state; whereas v<sup>0</sup> and u<sup>0</sup> species are derived from Ce 3d<sup>9</sup> 4f<sup>2</sup> O 2p<sup>5</sup> representing their final state [55]. Thus, the peaks labeled as u''' and v''' are linked to Ce<sup>4+</sup> species [56]. Then, O 1s spectrum confirms the presence of Ce<sup>3+</sup> as Ce<sub>2</sub>O<sub>3</sub> at 529.1 ± 0.2 eV, as well as peaks for TiO<sub>2</sub>, OH<sub>ads</sub>, and C–O (associated with carbonates compounds) were also observed at 530, 531.32, and 532.45 ± 0.2 eV, respectively [16]. Concerning the boron species, the B 1s region, Figure 3c, indicates the presence of B–O–Ti and B<sub>2</sub>O<sub>3</sub> interactions centered at 192.08 eV and 192.85 ± 0.2 eV. This interaction is mainly related to a synergistic effect with B<sup>3+</sup> species to promote the charge carrier separation, as established by the photocatalytic and photo-electrochemical experiments [26,36].

On the other hand, the emission peaks at 193.7 and 190.8 ± 0.2 eV could be due to the remaining H<sub>3</sub>BO<sub>4</sub> species from the doping reaction. The O 1s emission peak in TiO<sub>2</sub> is centered at 530.03 eV; whereas, the presence of B–O, Ti–O–B, and B<sup>3+</sup> signals, observed at 532.15 and 533.07 ± 0.2 eV, promotes the formation of oxygen vacancies. Table 2 and Table S2 show the full experimental composition (% wt.) calculated from B 1s, O 1s, Ce 3d<sub>3/2, 5/2</sub>, and Ti 2p signals.

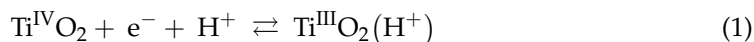
**Table 2.** Weight composition of O 1s, Ce 3d<sub>3/2, 5/2</sub>, and B 1s from the modified TiO<sub>2</sub>.

Species	TiO <sub>2</sub> -B		TiO <sub>2</sub> -Ce		
	Weight (%)	Bind Energy (eV)	Weight (%)	Bind Energy (eV)	
B 1s	B-N	6.59	190.8	-	-
	H <sub>3</sub> BO <sub>3</sub>	11.44	193.7	-	-
	B–O, BCO <sub>2</sub>	30.6	192.08	-	-
	B <sub>2</sub> O <sub>3</sub>	51.38	192.85	-	-
O 1s	TiO <sub>2</sub>	85.48	530.03	76.7	529.94
	B–O, Ti–O–B, Nitrates	3.99	532.15	-	-
	B <sup>3+</sup> (B <sub>2</sub> O <sub>3</sub> )	0.39	533.07	-	-
	Ce <sup>4+</sup> (CeO <sub>2</sub> )	-	-	3	528.51
	Ce <sup>3+</sup> (Ce <sub>2</sub> O <sub>3</sub> )	-	-	7.5	530.59
Ce 3d <sub>3/2, 5/2</sub>	Ce <sup>3+</sup>	-	-	72.8	885.7
	Ce <sup>4+</sup>	-	-	27.2	882.55

### 3.2. Photo-Electrochemical Studies

The current-potential responses of TiO<sub>2</sub> films, measured in sulfuric acid and dark conditions after 10 cyclic voltammetric scans at 50 mV/s, are shown in Figure S4. The dark current-potential characteristics are mainly dominated by the redox Ti<sup>4+</sup>/Ti<sup>3+</sup> (hydro)-oxide

species in the potential interval of 0.2 to  $-0.15$  V/RHE, Equation (1). This accumulation of electrons, in the conduction band of the oxide [57], reflects the doping degree effect of boron and cerium atoms in the oxide material, being more important with boron. These results are concomitant with Ti 2p XPS shown in Figure 3a:



The driving force of the system is displayed by the magnitude of the electrode potential, under illumination,  $\Delta E_{ph}$ . This parameter was measured in  $\text{H}_2\text{SO}_4$ , and  $\text{H}_2\text{SO}_4 + 0.5$  M  $\text{CH}_3\text{OH}$ . Methanol is usually used as a hole scavenger, and/or sacrificial agent in photocatalytic processes. In the experiment shown herein, in  $0.5$  M  $\text{H}_2\text{SO}_4$ , the magnitude of the photo-potential,  $\Delta E_{ph}$ , on  $\text{TiO}_2\text{-B}$  is higher than that of  $\text{TiO}_2$  and  $\text{TiO}_2\text{-Ce}$ . This trend is maintained in the presence of methanol, Table 3. It can be seen, however, that the initial OCP in darkness gives accounts on the electrolyte species interaction at the semiconducting electrode's surface, Figure 4a,b. The information obtained herein, via these simple experiments, titrate the ability of these non-modified, and modified semiconducting oxide to act as photocatalysts and/or photo-electrocatalysts.

**Table 3.** The open circuit potential data obtained in darkness, pseudo constant rates, and IPCE. Intensity of the lamp =  $30.8$   $\text{mW}/\text{cm}^2$ .

Sample	Photo-Potential ( $\Delta E_{ph}/\text{V}$ )		$k$ ( $\text{min}^{-1}$ )	IPCE (%)
	$0.5$ M $\text{H}_2\text{SO}_4$	$0.5$ M $\text{H}_2\text{SO}_4 + 0.5$ M $\text{CH}_3\text{OH}$		
P25	0.16	0.54	0.06	0.13
$\text{TiO}_2$	0.47	0.62	0.10	0.35
$\text{TiO}_2\text{-B}$	0.53	0.63	0.12	0.40
$\text{TiO}_2\text{-Ce}$	0.39	0.40	0.05	0.12

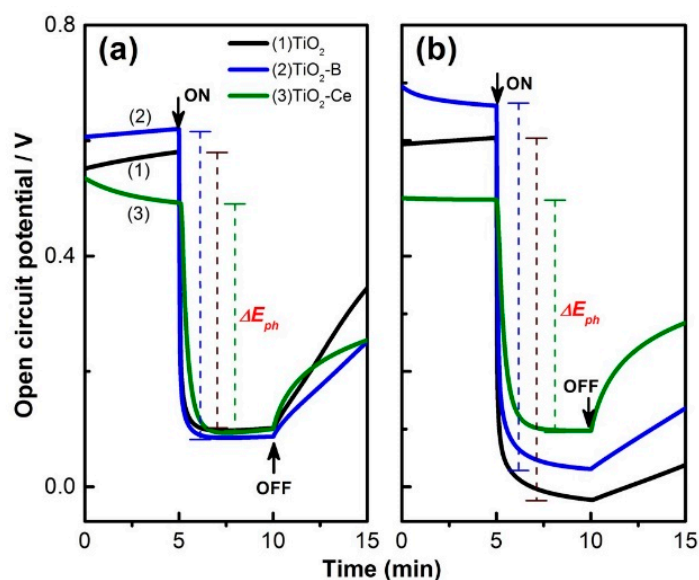


**Figure 4.** Open circuit potential (OCP) under dark and UV-Vis conditions, recorded during 15 min. (a)  $0.5$  M  $\text{H}_2\text{SO}_4$ , and (b)  $0.5$  M  $\text{H}_2\text{SO}_4 + 0.5$  M methanol. (1)  $\text{TiO}_2$ , (2)  $\text{TiO}_2\text{-B}$ , and (3)  $\text{TiO}_2\text{-Ce}$ .

Indeed, the photoelectrochemical results, shown in Figure S5, are concomitant to the data shown in Figure 4. In this latter, the magnitude of  $\Delta E_{ph}$  can be used as diagnostic for the material's photocatalytic activity. Moreover, the photocurrent-potential characteristic sheds additional light on the behavior of the material. As it is clearly observed, the

magnitude of the photocurrent,  $j_{ph}$ , and the onset potential with light is determined by the materials opto-electronic properties, as well as the nature of the species in the electrolyte.

In the absence of a hole-scavenger, Figure S5a, the magnitude of the photocurrent is limited by the hole charge transfer kinetics to adsorbed water, a mechanism known as an indirect path [58]. Herein, we observe that the boron-doped titania is more effective than the non-doped one. As stated in our earlier work [58], the direct interfacial charge transfer is favored with an effective hole scavenger, such as methanol. The presence of this small organics not only favors the separation of the photogenerated electron-hole pairs that occurs at more negative potentials, but the photocurrent is enhanced on all samples.

Herein, it is important to notice that the highest photocurrent is obtained on the boron-doped titania. Again, this is also concomitant with data displayed in Figure 4b. The observed onset potential shift amounts to  $-0.15$  V. In the presence of methanol, boron-doped and non-doped titania improve kinetics. This is not the case for cerium-doped titania, which remains at a similar electrode potential value without alcohol. The surface chemical nature of the materials, cf. Figure S5, might indicate that surface recombination centers present near the conduction band are deactivated in the presence of methanol. Moreover, the low photo-activity of cerium-doped titania could be due either to the presence of ceria cluster, and/or to the formation of nano-heterojunctions that block the photogenerated electron-hole pairs to be separated, even in presence of an important interfacial electrical field.

The description above is further clarified by the experiment under chopped light conditions, Figure 5A, which reflects the materials behavior reported in Figure S5. The aim, herein, was to visualize the charge separation at  $0.6$  V/RHE. While the response observed in Figure 5A is limited to the indirect charge transfer process, the methanol molecule puts in evidence that, indeed, under chopped conditions, the separation and/or recombination of photogenerated electron-hole pairs is slow on cerium-doped titania. The comparative results are summarized in the inset of Figure 5A. Positive as well as negative effects are, then, obtained by doping with boron and cerium, respectively, as also reflected by the results on the incident photon to current efficiency (ICPE), Figure 5B. The efficiency factor obtained is summarized in Table 3.

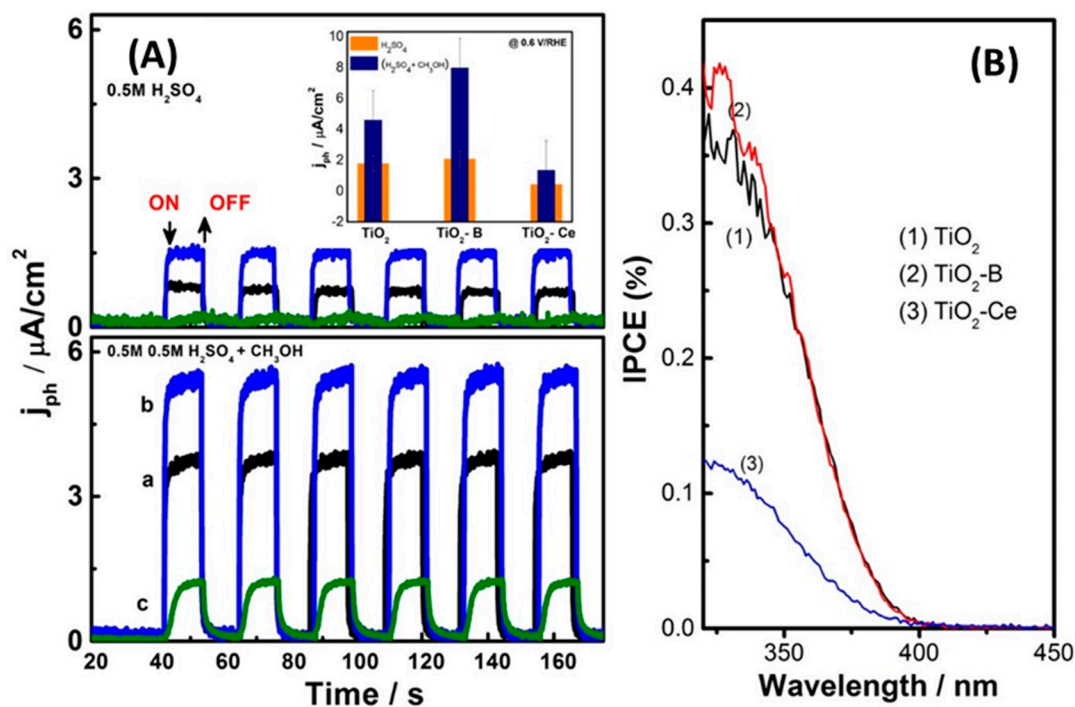


**Figure 5.** (A) Photocurrent response under chopped light (0.1 Hz) at  $0.6$  V/RHE on  $\text{TiO}_2$  (a),  $\text{TiO}_2\text{-B}$  (b), and  $\text{TiO}_2\text{-Ce}$  (c). Inset: Final ratio analysis in acid (orange) and acid + methanol (navy blue) reaction. (B) IPCE (incident photon to current efficiency) analysis obtained in acid + methanol, see data in Table 3. Mass deposited:  $0.2$   $\text{mg}/\text{cm}^2$ .

### 3.3. Photocatalysis

The photocatalytic activity of P25, TiO<sub>2</sub>, TiO<sub>2</sub>-B, and TiO<sub>2</sub>-Ce samples in powder form (333 mg/L), under UV-Vis illumination in presence of oxygen, as electron scavenger, was analyzed using as a dye: Reactive Black 5 (RB5) 40 mg/L. Prior to photocatalytic measurements, the dye was in contact with the samples, in the reactor, during 20 min under O<sub>2</sub> flow in darkness.

The dye UV-Vis absorption spectrum, curve (1), is shown in Figure 6c. The initial absorption,  $A_0$  at  $t_i = 0$  min is identified and taken at 600 nm. The absorption variation ( $A/A_0$ ) with time of the dye absorption is shown in Figure 6a. Based on the Langmuir-Hinshelwood model, the first 10 min the  $\log(A/A_0)$  with time follows a pseudo-first-order kinetics, equation (2) [59,60]. The rate constant,  $k$ , on each system can be represented by the straight yellow lines shown in Figure 6b and summarized in Table 3:

$$k = \frac{2.303}{t} \log\left(\frac{A_0}{A}\right). \quad (2)$$

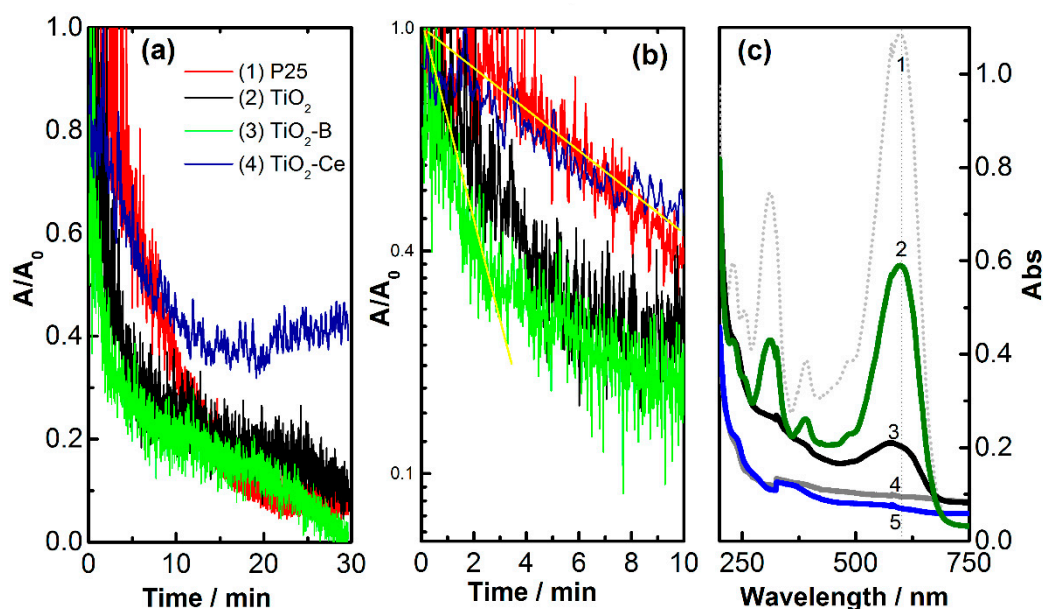


**Figure 6.** (a) Photo-discoloration of RB5 (Reactive Black 5) under UV-Vis light, (b)  $\log(A/A_0)$  vs.  $t$ , and (c) UV-Vis Reactive Black 5 (RB5) azo dye spectra,  $t_i = 0$  min curve (1); titrated at  $t = 30$  min, (curves 2–5). TiO<sub>2</sub> anatase (3) TiO<sub>2</sub>-B (5) and TiO<sub>2</sub>-Ce (2). P25 is a reference sample (4).

As shown in Figure 6c, the photo-discoloration efficiency of 94.5% on TiO<sub>2</sub>-B is higher than at P25 (90%), TiO<sub>2</sub> anatase (80%), and TiO<sub>2</sub>-Ce (42%). The boron-species through their surface oxidation-states might promote such a performance concomitant to the driving force (photo-potential), Figure 5, relatively higher compared to that of TiO<sub>2</sub> [20,33,61]. The presence of Ce<sup>4+</sup>/Ce<sup>3+</sup> species that leads to a low conversion rate can be attributed to the coexistence of such species, at the grain boundaries promoting a low separation efficiency of photo-induced carriers.

The discoloration rate of RB5 describes the photocatalytic activity in a stationary regime reactor. In regards to the BET surface, a fair comparison can indeed be done with the sol-gel generated materials, in which TiO<sub>2</sub>-B is more efficient than TiO<sub>2</sub> and TiO<sub>2</sub>-Ce.

### 4. Conclusions

The photo-electrocatalytic activity was investigated on oxide sol-gel generated samples: TiO<sub>2</sub> and boron-, and cerium-doped TiO<sub>2</sub>. The physical-chemical techniques (XRD, BET and SEM) revealed that samples were Anatase phase, nanometric crystals, with

mesopores morphologies. Surface analyses put, in addition, in evidence the presence of B-Ti-O and B<sub>2</sub>O<sub>3</sub> from B<sup>3+</sup> species. In a similar way, although more complex, Ce-Ti-O was also detected and put in evidence at the titania surface the presence of Ce<sup>4+</sup>/Ce<sup>3+</sup> redox species. This certainly conveyed to a different surface chemistry as shown via the photoelectrochemical responses. This in turn impacted the materials photocatalytic performance, in the sense that the charge separation is linked to the nature of the opto-electronic properties of semiconductor. It turned out, that the TiO<sub>2</sub>-B sample presented a better response in comparison with TiO<sub>2</sub> and TiO<sub>2</sub>-Ce. An effect that was reinforced by the presence of a hole-scavenger (methanol) in which the direct charge transfer path is favorable since it blocks the surface states present near the conduction band. These results further show that the implementation of semiconductors-based devices for redox reaction (i.e., hydrogen production) could be used as an alternative catalyst support for hydrogen production.

**Supplementary Materials:** The following are available online at <https://www.mdpi.com/2571-9637/4/1/8/s1>, Figure S1: (a) XRD diffraction pattern overview of P25, TiO<sub>2</sub>, B and Ce-doped anatase. (b) Rietveld analysis of TiO<sub>2</sub>, B and Ce-doped anatase. Inset: Fitting parameters on average R<sub>wp</sub>% (Weighted Rprofile), and GoF (Goodness of Fit). Figure S2: SEM morphologies of P25, TiO<sub>2</sub>, B and Ce-doped anatase. Figure S3: XPS general spectra of TiO<sub>2</sub> nanoparticles modified with boron and cerium: TiO<sub>2</sub>-B and TiO<sub>2</sub>-Ce. Figure S4: Current-potential characteristics of oxides deposited onto SnO<sub>2</sub>: F (FTO) in dark in 0.5M H<sub>2</sub>SO<sub>4</sub>. (a) FTO, (b) TiO<sub>2</sub> anatase, (c) TiO<sub>2</sub>-B, and (d) TiO<sub>2</sub>-Ce. Scan rate: 50 mV/s. Figure S5: Photocurrent-potential characteristics of doped-oxides (TiO<sub>2</sub>-B, and TiO<sub>2</sub>-Ce). Scan rate: 1 mV/s. The mass deposited on each sample was 0.2 mg/cm<sup>2</sup>. Table S1: Structural properties from Rietvel analysis for TiO<sub>2</sub>, TiO<sub>2</sub>-B and TiO<sub>2</sub>-Ce samples (cf. Figure SI-1(b)). Table S2: Weight composition of O1s, Ce3d<sub>3/2, 5/2</sub> and B1s collected from the modified TiO<sub>2</sub>.

**Author Contributions:** A.A.F.-C. carried out the experiments, analyzed the data, and wrote first version of the MS. A.M.-R. participated in the discussion—and funding acquisition. N.A.-V. conceived the experiments, wrote and corrected the manuscript. All authors have read and agreed to the published version of the manuscript.

**Funding:** This research was partially funded by CONACYT DEMS projects 160333, 247208 and IPN 20200507, 20210066 and the European Union (ERDF), “Région Nouvelle 430 Aquitaine”.

**Institutional Review Board Statement:** Not applicable.

**Informed Consent Statement:** Not applicable.

**Data Availability Statement:** Data is contained within the article or supplementary material.

**Acknowledgments:** A.A.F.-C. thanks CONACYT scholarship No. 397716 for the financial support for a year research internship at the University of Poitiers “BECAS MIXTAS 2016-MRZ 2017 MOVILIDAD EN EL EXTRANJERO (291062)”. The authors thank the CNMN-IPN for technical assistance, Angeles Hernández-Hernández from ESIQIE-IPN for valuable discussions, and Luis Alberto Estudillo Wong for the Rietvel analysis.

**Conflicts of Interest:** The authors declare no conflict of interest.

## References

1. Ma, Y.; Wang, X.; Jia, Y.; Chen, X.; Han, H.; Li, C. Titanium dioxide-based nanomaterials for photocatalytic fuel generations. *Chem. Rev.* **2014**, *114*, 9987–10043. [[CrossRef](#)] [[PubMed](#)]
2. Çelik, D.; Yıldız, M. Investigation of hydrogen production methods in accordance with green chemistry principles. *Int. J. Hydrog. Energy* **2017**, *42*, 23395–23401. [[CrossRef](#)]
3. Gupta, N.M. Factors affecting the efficiency of a water splitting photocatalyst: A perspective. *Renew. Sustain. Energy Rev.* **2017**, *71*, 585–601. [[CrossRef](#)]
4. Ahmad, A.L.; Yasin, N.H.M.; Derek, C.J.C.; Lim, J.K. Microalgae as a sustainable energy source for biodiesel production: A review. *Renew. Sustain. Energy Rev.* **2011**, *15*, 584–593. [[CrossRef](#)]
5. Tryk, D.A.; Fujishima, A.; Honda, K. Recent topics in photoelectrochemistry: Achievements and future prospects. *Electrochim. Acta* **2000**, *45*, 2363–2376. [[CrossRef](#)]
6. Fujishima, A.; Honda, K. Electrochemical photolysis of water at a semiconductor electrode. *Nature* **1972**, *238*, 37–38. [[CrossRef](#)]
7. Honda, K. Dawn of the evolution of photoelectrochemistry. *J. Photochem. Photobiol. A Chem.* **2004**, *166*, 63–68. [[CrossRef](#)]

8. Cargnello, M.; Gordon, T.R.; Murray, C.B. Solution-phase synthesis of titanium dioxide nanoparticles and nanocrystals. *Chem. Rev.* **2014**, *114*, 9319–9345. [[CrossRef](#)] [[PubMed](#)]
9. Chen, X. Introduction: Titanium dioxide (TiO<sub>2</sub>) nanomaterials. *Chem. Rev.* **2014**, *114*, 9281–9282.
10. Meng, Q.; Wang, T.; Liu, E.; Ma, X.; Ge, Q.; Gong, J. Understanding electronic and optical properties of anatase TiO<sub>2</sub> photocatalysts co-doped with nitrogen and transition metals. *Phys. Chem. Chem. Phys.* **2013**, *15*, 9549–9561. [[CrossRef](#)]
11. Chen, X.; Mao, S.S. Titanium dioxide nanomaterials: Synthesis, properties, modifications and applications. *Chem. Rev.* **2007**, *107*, 2891–2959. [[CrossRef](#)] [[PubMed](#)]
12. Clarizia, L.; Spasiano, D.; Di Somma, I.; Marotta, R.; Andreozzi, R.; Dionysiou, D.D. Copper modified-TiO<sub>2</sub> catalysts for hydrogen generation through photoreforming of organics. A short review. *Int. J. Hydrogen Energy* **2014**, *39*, 16812–16831. [[CrossRef](#)]
13. Asahi, R.; Morikawa, T.; Irie, H.; Ohwaki, T. Nitrogen-doped titanium dioxide as visible-light-sensitive photocatalyst: Designs, developments, and prospects. *Chem. Rev.* **2014**, *114*, 9824–9852. [[CrossRef](#)] [[PubMed](#)]
14. Fattakhova-Rohlfing, D.; Zaleska, A.; Bein, T. Three-dimensional titanium dioxide nanomaterials. *Chem. Rev.* **2014**, *114*, 9487–9558. [[CrossRef](#)]
15. Linsebigler, A.L.; Lu, G.; Yates, J.T. Photocatalysis on TiO<sub>2</sub> surfaces: Principles, mechanisms, and selected results. *Chem. Rev.* **1995**, *95*, 735–758. [[CrossRef](#)]
16. Shan, W.; Liu, F.; He, H.; Shi, X.; Zhang, C. A superior ce-w-ti mixed oxide catalyst for the selective catalytic reduction of NO<sub>x</sub> with NH<sub>3</sub>. *Appl. Catal. B Environ.* **2012**, *115*, 100–106.
17. Yang, S.; Kou, H.; Wang, H.; Cheng, K.; Wang, J. The photoelectrochemical properties of n<sub>3</sub> sensitized cati<sub>3</sub> modified TiO<sub>2</sub> nanocrystalline electrodes. *Electrochim. Acta* **2009**, *55*, 305–310. [[CrossRef](#)]
18. Ida, S.; Yamada, K.; Matsuka, M.; Hagiwara, H.; Ishihara, T. Photoelectrochemical hydrogen production from water using p-type and n-type oxide semiconductor electrodes. *Electrochim. Acta* **2012**, *82*, 397–401. [[CrossRef](#)]
19. De La Cruz, D.; Arévalo, J.C.; Torres, G.; Margulis, R.G.B.; Ornelas, C.; Aguilar-Elguézabal, A. TiO<sub>2</sub> doped with SM<sup>3+</sup> by sol-gel: Synthesis, characterization and photocatalytic activity of diuron under solar light. *Catal. Today* **2011**, *166*, 152–158. [[CrossRef](#)]
20. Myilsamy, M.; Murugesan, V.; Mahalakshmi, M. Indium and cerium co-doped mesoporous TiO<sub>2</sub> nanocomposites with enhanced visible light photocatalytic activity. *Appl. Catal. A Gen.* **2015**, *492*, 212–222. [[CrossRef](#)]
21. Li, F.B.; Li, X.Z.; Hou, M.F.; Cheah, K.W.; Choy, W.C.H. Enhanced photocatalytic activity of CE<sup>3+</sup>-TiO<sub>2</sub> for 2-mercaptobenzothiazole degradation in aqueous suspension for odour control. *Appl. Catal. A Gen.* **2005**, *285*, 181–189. [[CrossRef](#)]
22. Sidheswaran, M.; Tavlarides, L.L. Visible light photocatalytic oxidation of toluene using a cerium-doped titania catalyst. *Ind. Eng. Chem. Res.* **2008**, *47*, 3346–3357. [[CrossRef](#)]
23. Aman, N.; Satapathy, P.K.; Mishra, T.; Mahato, M.; Das, N.N. Synthesis and photocatalytic activity of mesoporous cerium doped TiO<sub>2</sub> as visible light sensitive photocatalyst. *Mater. Res. Bull.* **2012**, *47*, 179–183. [[CrossRef](#)]
24. Lee, S.M.; Lee, H.H.; Hong, S.C. Influence of calcination temperature on Ce/TiO<sub>2</sub> catalysis of selective catalytic oxidation of NH<sub>3</sub> to N<sub>2</sub>. *Appl. Catal. A Gen.* **2014**, *470*, 189–198. [[CrossRef](#)]
25. Grabowska, E.; Zaleska, A.; Sobczak, J.W.; Gazda, M.; Hupka, J. Boron-doped TiO<sub>2</sub>: Characteristics and photoactivity under visible light. *Procedia Chem.* **2009**, *1*, 1553–1559. [[CrossRef](#)]
26. Zaleska, A.; Grabowska, E.; Sobczak, J.W.; Gazda, M.; Hupka, J. Photocatalytic activity of boron-modified TiO<sub>2</sub> under visible light: The effect of boron content, calcination temperature and TiO<sub>2</sub> matrix. *Appl. Catal. B Environ.* **2009**, *89*, 469–475. [[CrossRef](#)]
27. Zaleska, A.; Sobczak, J.W.; Grabowska, E.; Hupka, J. Preparation and photocatalytic activity of boron-modified TiO<sub>2</sub> under uv and visible light. *Appl. Catal. B Environ.* **2008**, *78*, 92. [[CrossRef](#)]
28. Bettinelli, M.; Dallacasa, V.; Falcomer, D.; Fornasiero, P.; Gombac, V.; Montini, T.; Roma, O.D.L.; Speghini, A. Photocatalytic activity of TiO<sub>2</sub> doped with boron and vanadium. *J. Hazard. Mater.* **2007**, *146*, 529–534. [[CrossRef](#)] [[PubMed](#)]
29. Wong, M.-S.; Sun, M.-T.; Sun, D.-S.; Chang, H.-H. Visible-light-responsive antibacterial property of boron-doped titania films. *Catalysts* **2020**, *10*, 1349. [[CrossRef](#)]
30. Gražulis, S.; Chateigner, D.; Downs, R.T.; Yokochi, A.F.T.; Quirós, M.; Lutterotti, L.; Manakova, E.; Butkus, J.; Moeck, P.; Le Bail, A. Crystallography open database—An open-access collection of crystal structures. *J. Appl. Cryst.* **2009**, *42*, 726–729. [[CrossRef](#)]
31. Wu, C.Y.; Lee, Y.L.; Lo, Y.S.; Lin, C.J.; Wu, C.H. Thickness-dependent photocatalytic performance of nanocrystalline TiO<sub>2</sub> thin films prepared by sol-gel spin coating. *Appl. Surf. Sci.* **2013**, *280*, 737–744. [[CrossRef](#)]
32. Mao, D.; Lu, G. The effect of b<sub>2</sub>o<sub>3</sub> addition on the crystallization of amorphous TiO<sub>2</sub>-ZrO<sub>2</sub> mixed oxide. *J. Solid State Chem.* **2007**, *180*, 484–488. [[CrossRef](#)]
33. Lan, X.; Wang, L.; Zhang, B.; Tian, B.; Zhang, J. Preparation of lanthanum and boron co-doped TiO<sub>2</sub> by modified sol-gel method and study their photocatalytic activity. *Catal. Today* **2014**, *224*, 163–170. [[CrossRef](#)]
34. Li, S.; Zhu, H.; Qin, Z.; Wang, G.; Zhang, Y.; Wu, Z.; Li, Z.; Chen, G.; Dong, W.; Wu, Z.; et al. Morphologic effects of nano CeO<sub>2</sub>-TiO<sub>2</sub> on the performance of Au/CeO<sub>2</sub>-TiO<sub>2</sub> catalysts in low-temperature co oxidation. *Appl. Catal. B Environ.* **2014**, *144*, 498–506. [[CrossRef](#)]
35. Zhang, J.; Peng, W.; Chen, Z.; Chen, H.; Han, L. Effect of cerium doping in the TiO<sub>2</sub> photoanode on the electron transport of dye-sensitized solar cells. *J. Phys. Chem. C* **2012**, *116*, 19182–19190. [[CrossRef](#)]
36. Bilgin Simsek, E. Solvothermal synthesized boron doped TiO<sub>2</sub> catalysts: Photocatalytic degradation of endocrine disrupting compounds and pharmaceuticals under visible light irradiation. *Appl. Catal. B Environ.* **2017**, *200*, 309–322. [[CrossRef](#)]

37. Wang, Y.; Ren, J.; Liu, G.; Peng, P. Synthesis and characterization of iodine ion doped mesoporous TiO<sub>2</sub> by sol-gel method. *Mater. Chem. Phys.* **2011**, *130*, 493–499. [[CrossRef](#)]
38. Sreethawong, T.; Ngamsinlapasathian, S.; Yoshikawa, S. Surfactant-aided sol-gel synthesis of mesoporous-assembled TiO<sub>2</sub>-NiO mixed oxide nanocrystals and their photocatalytic azo dye degradation activity. *Chem. Eng. J.* **2012**, *192*, 292–300. [[CrossRef](#)]
39. Khan, R.; Kim, S.W.; Kim, T.J.; Nam, C.M. Comparative study of the photocatalytic performance of boron-iron co-doped and boron-doped TiO<sub>2</sub> nanoparticles. *Mater. Chem. Phys.* **2008**, *112*, 167–172. [[CrossRef](#)]
40. Feng, Q.; Chen, K.; Ma, D.; Lin, H.; Liu, Z.; Qin, S.; Luo, Y. Synthesis of high specific surface area silica aerogel from rice husk ash via ambient pressure drying. *Colloids Surf. A Physicochem. Eng. Asp.* **2018**, *539*, 399–406.
41. Mel'gunov, M.S.; Ayupov, A.B. Direct method for evaluation of bet adsorbed monolayer capacity. *Microporous Mesoporous Mater.* **2017**, *243*, 147–153. [[CrossRef](#)]
42. Muttakin, M.; Mitra, S.; Thu, K.; Ito, K.; Saha, B.B. Theoretical framework to evaluate minimum desorption temperature for iupac classified adsorption isotherms. *Int. J. Heat Mass Transf.* **2018**, *122*, 795–805. [[CrossRef](#)]
43. Zayadi, R.A.; Bakar, F.A. Comparative study on the performance of Au/F-TiO<sub>2</sub> photocatalyst synthesized from zamzam water and distilled water under blue light irradiation. *J. Photochem. Photobiol. A Chem.* **2017**, *346*, 338–350. [[CrossRef](#)]
44. Jiang, C.; Lee, K.Y.; Parlett, C.M.A.; Bayazit, M.K.; Lau, C.C.; Ruan, Q.; Moniz, S.J.A.; Lee, A.F.; Tang, J. Size-controlled TiO<sub>2</sub> nanoparticles on porous hosts for enhanced photocatalytic hydrogen production. *Appl. Catal. A Gen.* **2016**, *521*, 133–139. [[CrossRef](#)]
45. Singh, A.P.; Kumari, S.; Shrivastav, R.; Dass, S.; Satsangi, V.R. Iron doped nanostructured TiO<sub>2</sub> for photoelectrochemical generation of hydrogen. *Int. J. Hydrogen Energy* **2008**, *33*, 5363–5368.
46. Xue, X.; Wang, Y.; Yang, H. Preparation and characterization of boron-doped titania nano-materials with antibacterial activity. *Appl. Surf. Sci.* **2013**, *264*, 94–99. [[CrossRef](#)]
47. Ma, R.; Jahurul Islam, M.; Amaranatha Reddy, D.; Kim, T.K. Transformation of CeO<sub>2</sub> into a mixed phase CeO<sub>2</sub>/Ce<sub>2</sub>O<sub>3</sub> nanohybrid by liquid phase pulsed laser ablation for enhanced photocatalytic activity through z-scheme pattern. *Ceram. Int.* **2016**, *42*, 18495–18502. [[CrossRef](#)]
48. Viswanathan, B.; Raj, K.J.A. Effect of surface area, pore volume and particle size of p25 titania on the phase transformation of anatase to rutile. *Indian J. Chem. Sect. A Inorg. Phys. Theor. Anal. Chem.* **2009**, *48*, 1378–1382.
49. Rtimi, S.; Pulgarin, C.; Sanjines, R.; Nadtochenko, V.; Lavanchy, J.C.; Kiwi, J. Preparation and mechanism of cu-decorated TiO<sub>2</sub> films showing accelerated bacterial inactivation. *ACS Appl. Mater. Interfaces* **2015**, *7*, 12832–12839. [[PubMed](#)]
50. Zhang, W.; Xiao, X.; Zheng, L.; Wan, C. Fabrication of TiO<sub>2</sub>/MoS<sub>2</sub>@zeolite photocatalyst and its photocatalytic activity for degradation of methyl orange under visible light. *Appl. Surf. Sci.* **2015**, *358*, 468–478. [[CrossRef](#)]
51. Lee, J.M.; Kim, S.J.; Kim, J.W.; Kang, P.H.; Nho, Y.C.; Lee, Y.S. A high resolution xps study of sidewall functionalized mwcnts by fluorination. *J. Ind. Eng. Chem.* **2009**, *15*, 66–71. [[CrossRef](#)]
52. Radecka, M. TiO<sub>2</sub> for photoelectrolytic decomposition of water. *Thin Solid Film* **2004**, *451–452*, 98–104. [[CrossRef](#)]
53. Rtimi, S.; Baghriche, O.; Pulgarin, C.; Sanjines, R.; Kiwi, J. Design, testing and characterization of innovative TiN-TiO<sub>2</sub> surfaces inactivating bacteria under low intensity visible light. *RSC Adv.* **2012**, *2*, 8591–8595. [[CrossRef](#)]
54. Hench, L.L.; West, J.K. The sol-gel process. *Chem. Rev.* **1990**, *90*, 33–72. [[CrossRef](#)]
55. Bêche, E.; Charvin, P.; Perarnau, D.; Abanades, S.; Flamant, G. Ce 3d XPS Investigation of Cerium Oxides and Mixed Cerium Oxide (Ce<sub>x</sub>Ti<sub>y</sub>O<sub>z</sub>). *Surf. Interface Anal.* **2008**, *40*, 264–267. [[CrossRef](#)]
56. Tan, Y.; Zhang, S.; Shi, R.; Wang, W.; Liang, K. Visible light active Ce/Ce<sub>2</sub>O/CeO<sub>2</sub>/TiO<sub>2</sub> nanotube arrays for efficient hydrogen production by photoelectrochemical water splitting. *Int. J. Hydrogen Energy* **2016**, *41*, 5437–5444. [[CrossRef](#)]
57. Fabregat-Santiago, F.; Mora-Sero, I.; Garcia-Belmonte, G.; Bisquert, J. Cyclic voltammetry studies of nanoporous semiconductors. Capacitive and reactive properties of nanocrystalline TiO<sub>2</sub> electrodes in aqueous electrolyte. *J. Phys. Chem. B* **2003**, *107*, 758–768. [[CrossRef](#)]
58. Lana Villarreal, T.; Gómez, R.; Neumann-Spallart, M.; Alonso-Vante, N.; Salvador, P. Semiconductor photooxidation of pollutants dissolved in water: A kinetic model for distinguishing between direct and indirect interfacial hole transfer. I. Photoelectrochemical experiments with polycrystalline anatase electrodes under current doubling and absence of recombination. *J. Phys. Chem. B* **2004**, *108*, 20278–20290.
59. Zhang, J.; Huang, L.; Lu, Z.; Jin, Z.; Wang, X.; Xu, G.; Zhang, E.; Wang, H.; Kong, Z.; Xi, J.; et al. Crystal face regulating MoS<sub>2</sub>/TiO<sub>2</sub> (001) heterostructure for high photocatalytic activity. *J. Alloys Compd.* **2016**, *688*, 840–848. [[CrossRef](#)]
60. Gombac, V.; De Rogatis, L.; Gasparotto, A.; Vicario, G.; Montini, T.; Barreca, D.; Balducci, G.; Fornasiero, P.; Tondello, E.; Graziani, M. TiO<sub>2</sub> nanopowders doped with boron and nitrogen for photocatalytic applications. *Chem. Phys.* **2007**, *339*, 111–123. [[CrossRef](#)]
61. Panizza, M.; Cerisola, G. Electrocatalytic materials for the electrochemical oxidation of synthetic dyes. *Appl. Catal. B Environ.* **2007**, *75*, 95–101. [[CrossRef](#)]